Evaluation of advanced acoustic imaging methods for microphone-array measurements in closed-section wind tunnels

Merino Martinez, R.; VanDercreek, Colin; Snellen, M.

DOI
10.2514/6.2022-2810

Publication date
2022

Document Version
Final published version

Published in
28th AIAA/CEAS Aeroacoustics 2022 Conference

Aeroacoustics Conferences
June 14-17, 2022, Southampton, UK
28th AIAA/CEAS Aeroacoustics 2022 Conference

10.2514/6.2022-2810

Evaluation of advanced acoustic imaging methods for microphone–array measurements in closed–section wind tunnels

Roberto Merino-Martínez*[1], Colin VanDercreek†[1], and Mirjam Snellen‡[1]

[1]*Delft University of Technology, 2629 HS Delft, the Netherlands*

Aeroacoustic measurements with microphones in closed–section wind tunnels are typically hampered by the pressure fluctuations of the turbulent boundary layer (TBL) on the tunnel's walls, ceiling, or floor, where phased microphone arrays are usually mounted. This paper evaluates the performance of several advanced acoustic imaging methods that aim at overcoming this limitation for localizing and quantifying sound sources in closed–section wind–tunnel measurements. The acoustic data employed was obtained using a phased microphone array installed in two different configurations: flush–mounted on the wind–tunnel wall and recessed within cavities behind an acoustically transparent covering. The acoustic imaging methods considered are conventional frequency domain beamforming (CFDBF, as a baseline), functional (projection) beamforming (FUNBF), orthogonal beamforming (OB), CLEAN–SC, and the deconvolution approach for the mapping of acoustic sources (DAMAS). Two sound sources are analyzed: (1) a single speaker emitting broadband sound as a reference signal, and (2) a flat plate inside of the flow as a distributed aeroacoustic source. In general, it is observed that the array with cavities provides considerably better results as it benefits from a higher signal–to–noise ratio. In addition, removing the main diagonal from the cross–spectral matrix also helps obtaining clearer acoustic source maps and more accurate quantitative sound spectra estimations. Overall, DAMAS and OB are the best performing methods for the case with a single speaker. CFDBF and FUNBF are the most suitable methods for the case with the distributed sound source of the trailing edge of the flat plate, whereas the other techniques fail to properly identify it.

I. Introduction

Flow–generated sound plays an important role in the noise emissions of several industrial applications, such as aircraft [1, 2], ground vehicles [3], and wind turbines [4, 5]. The negative health effects caused by noise exposure and the ever stricter environmental noise regulations [6] motivate the design of quieter systems. To study flow–generated noise experimental testing is typically performed in (aeroacoustic) wind–tunnel facilities [7–9], which aim to reproduce in a controlled environment the flow conditions present in practice around the test model under analysis.

Typical test models in aeroacoustic experiments can be considerably complex systems, such as landing gears [10] or scaled aircraft models [11], consisting of numerous noise sources located in different positions and with diverse characteristics. In order to reduce noise emissions efficiently, it is essential to first obtain accurate information about the location and strength of all noise sources within these systems. Phased microphone arrays [12, 13] are widely employed for this task since, together with acoustic imaging algorithms [14], they allow for sound visualization and provide estimates of the location and strength of the different sound sources. Moreover, these devices considerably outperform the use of single microphones for acoustic measurements

*Assistant professor, Aircraft Noise & Climate Effects section, Faculty of Aerospace Engineering, Kluyverweg 1. AIAA Member. E-mail: r.merinomartinez@tudelft.nl

†PhD candidate, Aircraft Noise & Climate Effects section, Faculty of Aerospace Engineering, Kluyverweg 1. E-mail: c.p.vandercreek-1@tudelft.nl

‡Full professor, Aircraft Noise & Climate Effects section, Faculty of Aerospace Engineering, Kluyverweg 1. E-mail: m.snellen@tudelft.nl

in environments with high background noise levels, i.e. with a low signal–to–noise ratio (SNR), such as wind–tunnel facilities [15, 16]. This approach is also normally used to evaluate the performance of noise reduction measures [17–19].

Generally speaking, wind tunnel facilities can be divided into two main categories [14] depending on their test section:

- **Closed–section wind tunnels** typically entail lower corrections for model blockage and circulation with relatively better–controlled aerodynamic properties. Acoustic measurements can be performed non–intrusively by mounting microphones flush–mounted in the floor, ceiling, or walls of the wind tunnel [20], see Fig. 1 (left). However, the amplitudes of the near–field pressure fluctuations inside the turbulent boundary layer (TBL) developing along the wind–tunnel's floor, ceiling, or walls are generally much larger than the acoustic signals from the model. The effect of the TBL pressure fluctuations can be substantially attenuated by recessing the microphones in cavities covered by an acoustically transparent perforated plate or wire mesh at some distance from the TBL [16, 21–24], see Fig. 1 (right). Additional challenges present in this configuration involve typically high background noise levels from the wind–tunnel circuit [25] and sound reflections from the solid surfaces of the test section that can lead to erroneous measurements of the sound levels emitted by the model [26, 27].

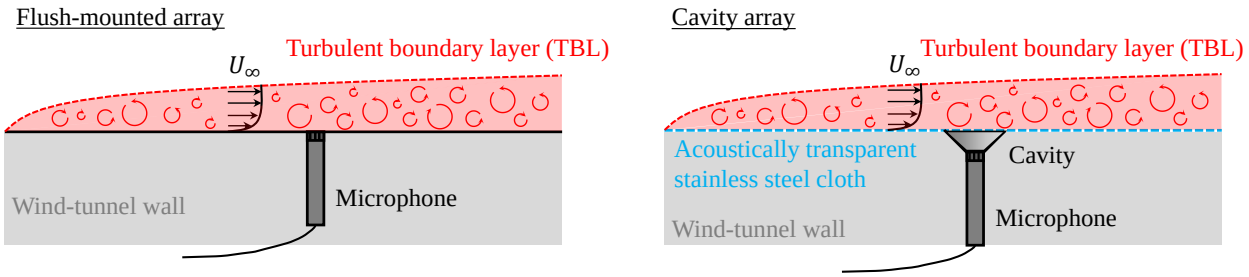

Figure 1: Diagram explaining the two considered configurations for placing microphones on a wind–tunnel wall (or floor or ceiling): (left) flush–mounted microphones, (right) recessed microphones in cavities covered by an acoustically transparent cloth.

- **Open–jet wind tunnels:** are characterized by the formation of a jet shear layer from the wind–tunnel nozzle's exit. The main advantages from this configuration is that the microphones and other instrumentation can be placed non–intrusively outside the flow, not being subject to turbulence and that the background noise levels are typically lower than in the closed–section counterparts. Furthermore, the test chamber surrounding the jet is usually acoustically treated with acoustic absorbing foam wedges, so that most sound reflections are suppressed [28]. These benefits usually make this type of configuration preferred in case accurate far–field sound pressure levels (L_p) estimates are of interest [9]. On the other hand, due to the jet spreading, the flow quality and alignment are generally more difficult to be controlled and corrections are required for obtaining the effective angle of attack and effective aerodynamic coefficients [29]. Acoustic effects, such as the refraction through the shear layer [30], also need to be accounted for, especially when considering the distortion in phase of the acoustic signals recorded by microphones [31, 32] and the spectral broadening due to the shear layer turbulence [33].

A compromise solution is a hybrid wind tunnel configuration, which consists in replacing the hard wind–tunnel walls of the closed–section configuration with acoustically transparent walls, such as tensioned Kevlar sheets [34], like in the stability tunnel of the Virginia Polytechnic Institute and State University [35, 36] or the Poul la Cour wind tunnel of the Technical University of Denmark. This hybrid configuration has the advantages of both closed–section (better controlled aerodynamic properties) and open–jet wind tunnels (placement of the microphones and instrumentation outside the flow), but the conversion of currently existing facilities into hybrid wind tunnels can become a challenging and costly process. A recent study by Sanders *et al.* [37] compared airfoil trailing–edge noise measurements performed in three test section configurations (closed, open–jet, and hybrid) in the same wind tunnel facility and observed differences of about ±3 dB between the far–field noise levels measured in each configuration. In particular, the PhD thesis of Kröber

[38] investigated the comparability of microphone array measurements in open–jet and closed–section wind tunnels.

Some of the aforementioned issues present in either wind–tunnel configuration can be (partially) mitigated using postprocessing techniques [15, 26, 27, 39–41]. In fact, a long list of advanced acoustic imaging methods [14, 42] have been tailored to specifically alleviate some of these shortcomings, as well as other practical limitations inherent to phased array processing [7] (e.g. the presence of sidelobes and limited spatial resolution). Previous benchmark exercises [43–45] showed that different methods provided considerably different results.

The objective of the current study is to evaluate the performance of several advanced acoustic imaging methods (see section II) for localizing and quantifying sound sources in closed–section wind–tunnel measurements. The experimental setup employed corresponds to the study performed by VanDercreek *et al.* [24], which also investigated different cavity geometries to recess the array microphones and obtain improved acoustic measurements. The current paper considers two configurations for the array microphones: flush–mounted on the wind–tunnel wall (as baseline) and recessed in the best–performing cavity geometry from [24] behind an acoustically transparent covering. The main idea is that such a cavity array can be implemented in already–existing closed–wall wind tunnels in an easier way compared to fully converting the whole facility to a hybrid wind tunnel. Two experimental test cases are considered: (1) a single speaker emitting broadband sound as a reference known signal, and (2) a flat plate inside of the flow as a distributed aeroacoustic source.

Section II briefly describes the acoustic imaging methods considered. The experimental setup is explained in section III. The main results are presented and discussed in section IV and the conclusions are listed in section V.

II. Acoustic imaging methods

II.A. Conventional frequency domain beamforming (CFDBF)

Conventional frequency domain beamforming (CFDBF) [46] is a method based on the phase differences between the signals recorded by each microphone of the array. It considers a scan grid of potential sound sources and performs an exhaustive search: for each grid point, the agreement between the expected solution for a sound source at that location and the actual signals recorded by the array microphones is assessed. This method is widely–used since it is robust, intuitive, and computationally inexpensive. However, CFDBF is influenced by the array's point spread function (PSF), i.e. the array's response to a unitary point source, which is limited by the Rayleigh resolution limit [47], i.e., the minimum distance at which two sound sources can be distinguished, and is subject to high sidelobe levels (spurious sources), especially at high frequencies.

To quantify the sound emissions by spatially distributed sources, integration methods that aim to reduce the influence of the array's PSF, such as the Source Power Integration (SPI) technique and its variants [12, 48–50], are typically applied over the region of integration (ROI) under analysis.

All the results previously presented in [24] were obtained using CFDBF.

II.B. Functional beamforming (FUNBF)

Functional beamforming (FUNBF) [51] provides a higher dynamic range (or lower sidelobe level) and array spatial resolution than CFDBF. Essentially, this technique consists in raising the autopowers of the CFDBF source map (see section II.A) to the power of an exponent parameter ν and the cross–spectral matrix (CSM) [12] to the inverse of this power $1/\nu$ to maintain the source levels. For this paper, the value of ν was selected to be 8 after performing a sensitivity analysis [52, 53].

Functional beamforming source maps can be integrated in a similar way as those from CFDBF using an adapted version of SPI [10, 54, 55]. Moreover, a novel integration method called functional projection beamforming (FPB) was recently proposed [56]. FPB characterizes a ROI of a FUNBF source map as a subspace in the array steering vector space and projects the acoustic data (namely the CSM) onto this subspace to yield the emitted sound spectrum within that ROI. This technique has shown promising results in preliminary benchmark exercises compared to other acoustic imaging methods [56–58]. In this paper, the performance of FPB is studied using a sum value ($\tilde{s}_0$ in [58]) of 0.9 that defines the proportion of expected significant singular values was employed [56, 58] (i.e. those that contain 90% of the energy contained in all singular values).

II.C. Orthogonal beamforming (OB)

Orthogonal beamforming (OB) [59], similarly to FUNBF, is also based on the eigenvalue decomposition of the CSM. It builds on the idea of separating the signal (incoherent sound sources) and the noise (non–acoustic pressure fluctuations, such as those from the TBL) subspaces [60].

OB considers a matrix $\boldsymbol{G}$ consisting of the steering vectors between the incoherent sound sources and the array microphones. The main idea behind OB is that each eigenvalue of $\boldsymbol{G}$ can be used to estimate the absolute source level of one source, from the strongest sound source within the map to the weakest, assuming orthogonality between steering vectors. These sources are then mapped to specific locations by assigning the eigenvalues to the location of the highest peak in a special beamforming source map constructed from a rank–one CSM synthesized from the corresponding eigenvector.

An important parameter, which has to be adjusted by the user, is the number of eigenvalues that span the signal subspace, which can be estimated by observing the number of dominant eigenvalues of the CSM. In this paper, the number of eigenvalues was defined in a flexible way as those whose sum contains the 90% of the trace of the matrix.

II.D. CLEAN-SC

CLEAN–SC [61] is a well–known frequency domain deconvolution technique that uses the fact that sidelobes are spatially coherent with the main lobe [61]. CLEAN–SC is based on the assumption that the CSM can be written as a summation of contributions from incoherent sources. The CLEAN–SC algorithm starts by finding the steering vector yielding the maximum value of the CFDBF source map. The contribution of the source component corresponding to that steering vector is then multiplied by a loop gain factor $\tilde{\varphi}$ between 0 and 1 (selected as 0.99 in this paper) and subtracted from the CSM and, afterward, the same procedure is repeated for the remaining CSM, until a certain stop criterion is fulfilled [61]. Ideally, the remaining CSM is "empty" after the iterative process. In other words, its norm should be small compared to the one of the original CSM. The new source map is obtained by the summation of the clean beams of the identified sound sources and the remaining degraded CSM [62].

This method has a relatively low sensitivity to errors made in the source model that describe the sound propagation, i.e., if the steering vectors considered do not exactly match with the source vectors [63]. The source maps obtained by the CLEAN–SC methods can be integrated to obtain a sound spectrum by simply adding the powers of the deconvoluted *clean* sources calculated within a predefined ROI [61].

II.E. Deconvolution approach for the mapping of acoustic sources (DAMAS)

The Deconvolution Approach for the Mapping of Acoustic Sources (DAMAS) [64] attempts to remove the influence of the array geometry and aperture from the output of CFDBF. DAMAS considers incoherent point sources located at the grid points and attempts to determine each source power by solving the inverse sound propagation problem subject to the constraint that source powers are non–negative. The problem is typically solved using a Gauss–Seidel iterative method (although alternative faster approaches based on sparsity are also possible [14]), which typically requires thousands of iterations to provide a "clean" source map [64]. For practical grids, the number of grid points is large and the size of the system of equations to be solved can become an issue. The computation time of DAMAS employed this way is proportional to the third power of the number of grid points. In addition, DAMAS has no mechanism to let the iteration converge towards a well–defined result and the solution may depend on how the grid points and the initial values are ordered. In this study, a total of 5000 iterations were employed.

II.F. Overview of the acoustic imaging methods employed

All the acoustic imaging methods mentioned above consider the steering vector formulation suggested by Sijtsma [12] and a spacing between grid points in the two–dimensional scan plane of $\Delta x = \Delta y = 1$ mm, except for DAMAS which has a coarser grid with $\Delta x = \Delta y = 50$ mm. Table 1 contains a overview of the relevant parameters selected in this paper. The ROIs employed for quantifying the noise emissions are described in section III for each test case.

Table 1: Overview of the relevant parameters selected for the acoustic imaging methods employed.

Acoustic imaging method	Relevant parameters
CFDBF	Steering vector formulation suggested by Sijtsma [12]
FUNBF	Exponent $\nu = 8$
FPB	Exponent $\nu = 8$, sum value $\tilde{s_0} = 0.9$
OB	Number of eigenvalues that contain 90% of the matrix trace
CLEAN–SC	Loop gain factor $\tilde{\varphi} = 0.99$
DAMAS	Gauss–Seidel solver with 5000 iterations and coarser grid $\Delta x = \Delta y = 0.05$ m

II.F.1. Diagonal removal

The performance of all the acoustic imaging methods considered was also evaluated in combination with the diagonal removal (DR) technique [14]. This approach replaces the diagonal elements of the CSM (i.e. the microphone auto–correlations) with zero values in order to neglect the contribution of noise which is incoherent for all the array microphones. This technique is especially useful (and often necessary) for cases with wind noise or TBL noise, such as in closed–section wind tunnels [7, 12].

III. Experimental setup

III.A. Wind–tunnel facility

The experiments were performed in the anechoic open–jet wind–tunnel facility of Delft University of Technology (A–tunnel) [28]. Despite being an open–jet wind tunnel, the current experimental setup aimed to reproduce the conditions present in practice for microphone arrays in closed–section wind tunnels, such as a TBL development along the wall. This was achieved by extending one of the edges of the rectangular nozzle with a 1.1 m × 0.4 m plate in which the microphones were mounted, see Fig. 2a. With this geometry, the sound perceived by the microphones is dominated by the TBL noise over the array, as would be the case in a closed–section wind tunnel. This setup also allowed for the speaker employed as a reference test case to be placed outside of the flow, avoiding the interaction of the flow with the speaker and its support structure, which would generate additional unwanted noise sources.

The test section of the A–Tunnel is located within an anechoic plenum that measures 6.4 m (length) × 6.4 m (width) × 3.2 m (height). The chamber is covered with acoustic absorbing foam wedges, which provide free–field sound propagation properties for frequencies higher than 200 Hz [28], thus reducing unwanted reflections from walls, floor, and ceiling. The rectangular nozzle employed has an exit area of 0.7 m × 0.4 m, see Fig. 2a, and provides a maximum flow velocity, U_∞, of 34 m/s. For this experiment flow velocities of 20 m/s and 34 m/s were considered. Hot–wire anemometry measurements in six relevant locations on the array plate confirmed that the boundary layer was turbulent and attached for both flow velocities and both array configurations. For more detailed information the reader is referred to [24].

Figure 2a also depicts the coordinate system used henceforth, centered in the array's center (which is also aligned with the jet axis), with the x axis in the streamwise direction, the y axis pointing left, and the z axis pointing towards the speaker.

III.B. Microphone array

The phased array consists of 16 *G.R.A.S. 40PH* analog free-field microphones [65] with two additional flush–mounted reference microphones at $((x, y) =$ (-0.4 m, 0 m) and $((x, y) =$ (0 m, 0 m), see Fig. 2a. The microphone array was installed in the aforementioned 1.1 m × 0.4 m poly–carbonate plate flush–mounted to one of the exit edges of the nozzle, see Fig. 2a.

The microphone configuration was optimized in a sunflower pattern [66] with a diameter of approximately 350 mm, see Fig. 2b. The center of the microphone distribution ($x = y = z = 0$ m) is located 800 mm downstream of the nozzle exit plane, see Fig. 2a, in order to allow for the boundary layer along the plate to become fully turbulent. The selected microphone configuration is meant to minimize sidelobes and maximize

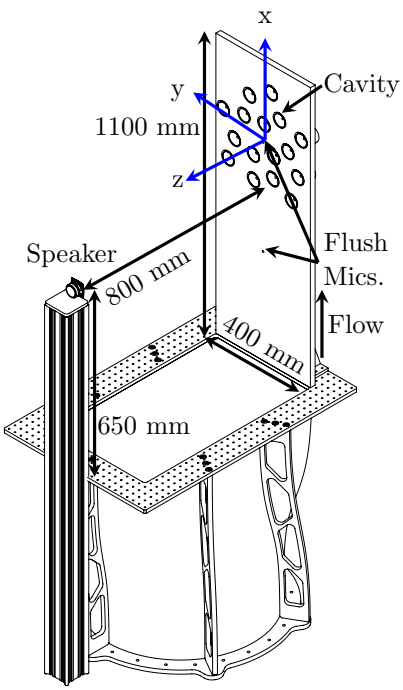

(a)

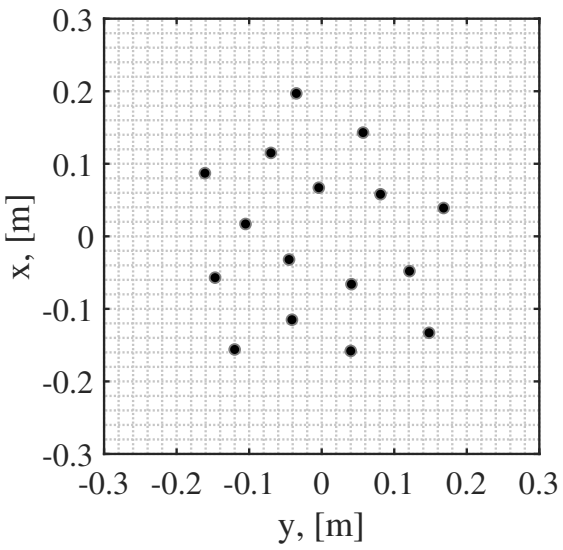

(b)

Figure 2: (a) Experimental setup at the A–tunnel with the microphone array mounted on the plate flush–mounted to the one of the exit edges of the nozzle. Adapted from [24]. (b) Microphone distribution as seen from the back of the plate.

the dynamic range between 2 kHz and 4 kHz. This design was predicted to have a maximum dynamic range of 9.6 dB and, due to its relatively small size, a usable frequency range from approximately 1 kHz to 9.2 kHz [24].

All microphones were calibrated individually using a *G.R.A.S. 42AA* pistonphone [67] following the guidelines of Mueller [7]. The microphones have a flat frequency response within ±1 dB from 50 Hz to 5 kHz and within ±2 dB from 5 kHz to 20 kHz. The data acquisition system consisted of four *National Instruments (NI) PXIe–4499* sound and vibration modules with 24 bits resolution. The boards are controlled by a *NI RMC–8354* computer via a *NI PXIe-8370* board. The sampling frequency was 51.2 kHz and the recording time 45 s.

For all acoustic imaging methods, the CSM is calculated using 4096 samples with a 50% overlap using Hanning windowing. The scan grids employed were located at the expected source location from the array plane, i.e. at the speaker baffle plane (z = 800 mm) and at the flat plate trailing edge (z = 350 mm), respectively, and had dimensions of 1 m × 1 m centered at the expected source location, see section III.D. The acoustic spectra, shown in subsequent sections in one–third–octave bands, are presented for the frequencies between 1 kHz and 10 kHz, due to the array and speaker limitations.

III.C. Microphone cavities

Two different array configurations [24] were employed, each of them mounted in a different plate of the same dimensions:

1. A reference configuration with the microphones flush–mounted to the poly–carbonate plate with holes of the same diameter as the *G.R.A.S. 40PH* microphones (7 mm).

2. A configuration with recessed cavities covered with an acoustically transparent stainless steel cloth with a thread diameter of 0.025 mm and 500 thread per square inch (#500). In this plate, the cavities are installed in threaded holes of 50 mm diameter at the microphone positions. This configuration

allowed for different cavity geometries to be tested [24]. The cavities considered in this paper are derived from a confidential design and have a conical shape with its walls made of acoustic absorbing melamine foam.

Figure 3a depicts the one–third–octave band frequency spectra of the single speaker (see section III.D) averaged over all the microphones in both array configurations (without any flow velocity) as solid lines. It is observed that the array with cavities (in red) measures lower L_p values throughout the spectra, especially for higher frequencies with differences up to -9.3 dB for the 10 kHz band. This reduction is believed to be because the sound–absorbing foam and the location of the microphone within the foam reduces the sound reflections with the cavity compared to the pressure doubling seen for the flush–mounted microphones [68]. In the same figure are also presented the TBL noise spectra (also in one–third–octave bands) measured by both array configurations for both flow velocities considered, $U_\infty = 20$ m/s and 34 m/s, as dashed and dotted lines, respectively. The array with cavities manages to effectively reduce the measured TBL noise up to 42 dB for the higher frequency bands with respect to the flush–mounted array baseline. The reductions of the overall sound pressure level ($L_{p,overall}$) for the whole frequency range considered (1 kHz to 10 kHz) are 28.5 dB and 23.3 dB for $U_\infty = 20$ m/s and 34 m/s), respectively.

The combination of both effects leads to an increase of the SNR (defined as $L_{p,speaker} - L_{p,TBL}$) of the signal measured by the array with cavities with respect to the flush–mounted array baseline of between 20 dB and 35 dB for different frequency bands, see Fig. 3b.

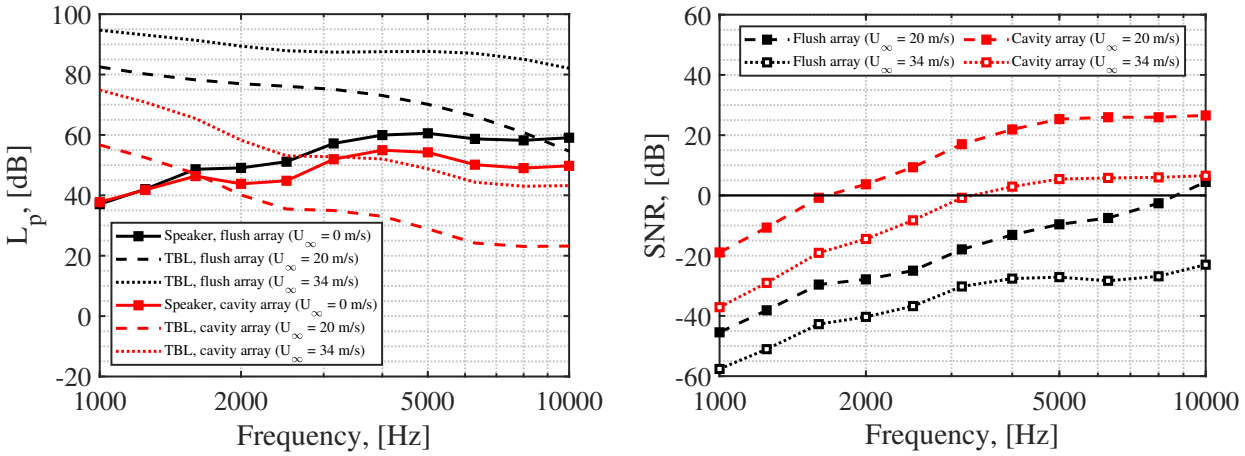

(a) (b)

Figure 3: (a) Average one–third–octave band frequency spectra of the single speaker (without flow) as well as the TBL noise spectra (with speaker off) for the flow velocities of $U_\infty = 20$ m/s and 34 m/s for both array configurations. (b) Signal–to–noise ratio (SNR) of the speaker signal for both flow velocities and both array configurations.

III.D. Sound sources

Two different sound sources were tested as benchmark cases to evaluate the performance of the acoustic imaging methods:

1. A single Visaton K 50 SQ speaker [69] located 800 mm away from the array plane in the z direction and 650 mm downstream from the nozzle outlet (i.e. at $x = -150$ mm) and aligned with the jet axis (i.e. $y = 0$ mm), see Fig. 2a. This position is outside of the flow to avoid additional noise sources due to shear layer impingement. The speaker has a baffle diameter of 45 mm and an effective piston area of 12.5 cm^2. Its frequency response ranges between 250 Hz and 10 kHz and it has a maximum power of 3 W. The speaker was employed to emit broadband noise with an $L_{p,overall}$, measured at the array center (without flow), of 64 dB. The average one–third–octave band spectra of all the microphones of both array configurations are depicted in Fig. 3a, as well as the respective SNR with respect to the TBL noise in Fig. 3b. The SNR varied considerably for different frequencies, flow velocities, and microphone array configurations, ranging from a minimum of about -57 dB, for the flush–mounted

array at 1 kHz and 34 m/s, to about 26 dB for the cavity array at 10 kHz and 20 m/s. For acoustic imaging, the frequency spectra of the emitted sound by the speaker were calculated by integrating the source maps within a 200 mm × 200 mm ROI centered at the speaker, i.e. (x, y) = (-150 mm, 0 mm), see Figs. 5 and 6.

2. A flat plate placed inside of the flow and mounted along the jet axis (z = 350 mm) and held by two support plates perpendicular to the plate in which the microphone array was mounted, as shown in Fig. 4a. The flat plate was 0.4 m wide and 1 m long and was set at 0° angle of attack. In this configuration, the test model is expected to have a distributed sound source along its trailing edge. The trailing edge had a thickness of 1 mm and was located at x = 160 mm. The flat plate was tripped at 5% of the chord from the leading edge and the estimated boundary layer displacement thickness at the trailing edge δ^* is 2.8 mm [24]. This plate was chosen to provide a more representative test case for aeroacoustic applications. Figure 4b depicts the SNR of the flat plate signal (defined as $L_{\mathrm{p,flat\ plate}} - L_{\mathrm{p,TBL}}$) for both flow velocities and array configurations (note the different scale in the y-axis compared to Fig. 3b). Once again, the array with the microphones recessed in cavities provides a higher SNR throughout the whole frequency spectrum than the flush–mounted array, except for the one–third–octave frequency bands centered at 1 kHz and 1.25 kHz at U_∞ = 34 m/s. The reason why the flush–mounted array provides a higher SNR in these cases is not yet clear, but could be due to the aforementioned signal reduction because of the sound–absorbing foam [68]. For acoustic imaging, the frequency spectra of the emitted sound by the trailing edge of the flat plate were calculated by integrating the source maps within a 200 mm × 200 mm ROI centered at the middle of the trailing edge, i.e. (x, y) = (160 mm, 0 mm).

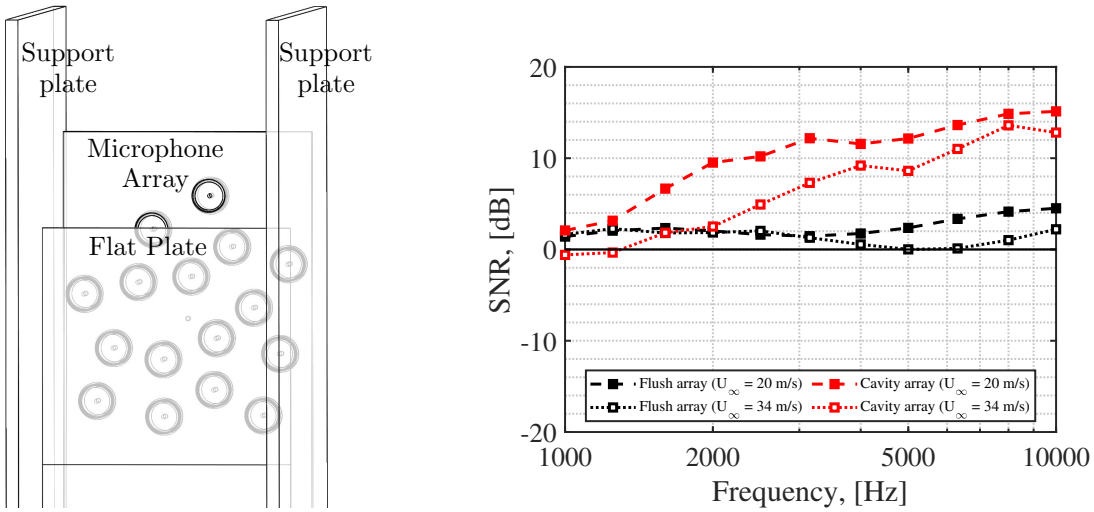

(a) (b)

Figure 4: (a) Illustration of the flat plate mounted between support plates with the array with microphone cavities depicted [24]. (b) Signal–to–noise ratio (SNR) of the flat plate signal for both flow velocities and both array configurations.

IV. Results and discussion

The results presented are divided depending on the noise source present: the single speaker IV.A and the flat plate IV.B. Some exemplary acoustic source maps are depicted, as well as the integrated sound spectra for each flow velocity and array configuration.

IV.A. Single speaker

IV.A.1. Acoustic source maps

Two example cases are considered for the analysis of the source maps obtained by each acoustic imaging method. Figures 5 and 6 contain the acoustic source maps for the single speaker emitting broadband sound with a flow velocity of 34 m/s and one–third–octave frequency bands centered at 1600 Hz and 10 kHz, respectively. These frequency bands represent some of the lowest and highest SNR cases for both arrays. In both figures, different rows correspond to different acoustic imaging methods CFDBF (a–d), FUNBF (e–h), OB (i–l), CLEAN–SC (m–p), and DAMAS (q–t), whereas the different columns correspond to different array configurations and the use of DR or not. In this way, the first two columns correspond to results obtained by the flush–mounted array without DR (first column) and with DR (second column) whereas the last two columns correspond to results obtained by the cavity array without DR (third column) and with DR (fourth column). For each source map, the ROI is depicted as a dashed magenta square and the speaker baffle as a green circle.

The case with 1600 Hz in Fig. 5 and $U_\infty = 34$ m/s has a SNR of about -42.7 dB and -19 dB for the flush–mounted and cavity arrays, respectively (see Fig. 3b. Due to such a low SNR value, none of the acoustic imaging methods (even with DR) applied to the data recorded by the flush–mounted array is able to properly localize the speaker as a sound source and all maps are heavily contaminated by TBL noise. Only DAMAS without DR (Fig. 5q) seems to detect a cluster of sound sources around the speaker location (as well as other sources in the perimeter of the scan grid) but, based on source maps on neighboring frequency bands (not shown here), this could be just a coincidence. The analogous results obtained by the array with the microphones recessed in cavities (last two columns in Fig. 5) are similar to those by the flush–mounted array if DR is not applied (third column), but they considerably improve once DR is applied. In fact, both CFDBF (Fig. 5d) and FUNBF (Fig. 5h) are able to successfully localize the speaker as a sound source, although with a limited spatial resolution (wide main lobe). The odd–looking source maps of FUNBF combined with DR (e.g. Fig. 5h) are due to the sensitivity of this method to DR [70] since it strongly depends on the eigenvalue decomposition of the CSM. OB (Figs. 5k and l) does not manage to properly detect the speaker. CLEAN–SC localizes two noise sources on the lower corners of the scan grid and only detects a weaker source within the ROI once DR is applied. DAMAS seems to outperform the rest of methods for the cavity array cases (Figs. 5s and t), especially once DR is applied, which manages to clear some of the noise sources present in the scan grid perimeter in the case without DR.

Conversely, the case with a frequency band of 10 kHz in Fig. 6 and $U_\infty = 34$ m/s has a SNR of about -23 dB and 6.5 dB for the flush–mounted and cavity arrays, respectively (see Fig. 3b. The higher SNR compared to the case with 1600 Hz from Fig. 5 allows for the localization of the speaker (although heavily contaminated by spurious sources) by CLEAN–SC (Fig. 6n) and DAMAS (Fig. 6r) when DR is applied to the data recorded by the flush–mounted array. If the cavity array is employed (last two columns in Fig. 6) all acoustic imaging methods are able to properly localize the speaker. In this case, CLEAN–SC (Figs. 6o and p) provides the clearest source maps, with essentially no sidelobes present for the color range selected (20 dB). FUNBF (Figs. 6g and h) and DAMAS (Figs. 6s and t) obtain slightly *dirtier* maps that still present some spurious sources outside of the ROI. Lastly, CFDBF (Figs. 6c and d) and OB (Figs. 6k and l) are also able to detect the speaker but perform considerably worse than the other methods due to the high presence of sidelobes (especially for OB) and poorer spatial resolution.

In order to observe in an easier way the overall performance of each acoustic imaging method (with and without DR) in terms of sound source localization for both array configurations and flow velocities, Fig. 7 depicts the one–third–octave frequency bands for which the speaker was clearly detected in the acoustic source maps. For the flush–mounted array with a flow velocity of 20 m/s (Fig. 7a) all methods without DR are able to detect the source for frequencies higher than 5 kHz. Applying DR enables the detection for the two frequency bands below (3150 Hz and 4 kHz). Additionally, CLEAN–SC and DAMAS are able to detect the speaker for lower frequencies, such as 1600 Hz. However, for the higher flow velocity (34 m/s, Fig. 7c), only DAMAS is able to detect the speaker without the aid of DR for some frequency bands. In this case, the application of DR enables the source identification, but only for the highest frequencies. Only CLEAN–SC is able to consistently detect the speaker for frequencies higher than 5 kHz. For the case with the cavity with recessed microphones within cavities and a flow velocity of 20 m/s (Fig. 7b), the lowest frequency band for which all the methods are able to detect the speaker is considerably extended until 1600 Hz. Some methods, like CLEAN–SC, are even able to detect the source for frequency bands as low as 630 Hz and

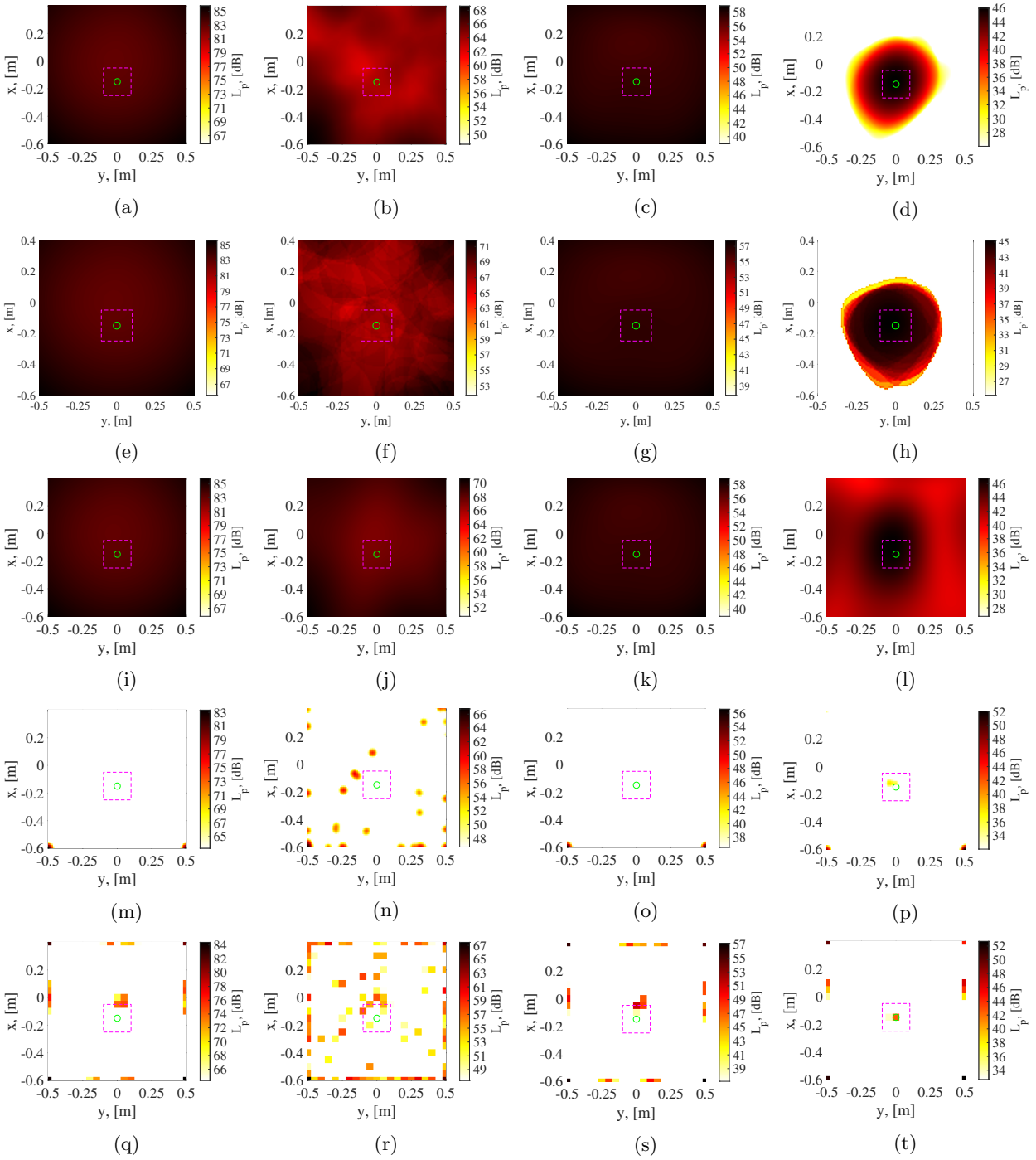

Figure 5: Acoustic source maps for the single speaker for $U_\infty = 34$ m/s and a one–third–octave frequency band centered at 1600 Hz. The first two columns correspond to results obtained by the flush–mounted array without DR (first column) and with DR (second column) whereas the last two columns correspond to results obtained by the cavity array without DR (third column) and with DR (fourth column). The rows correspond to for: CFDBF (a–d), FUNBF (e–h), OB (i–l), CLEAN–SC (m–p), and DAMAS (q–t). The dashed magenta squares denote the ROI and the green circle denotes the speaker baffle.

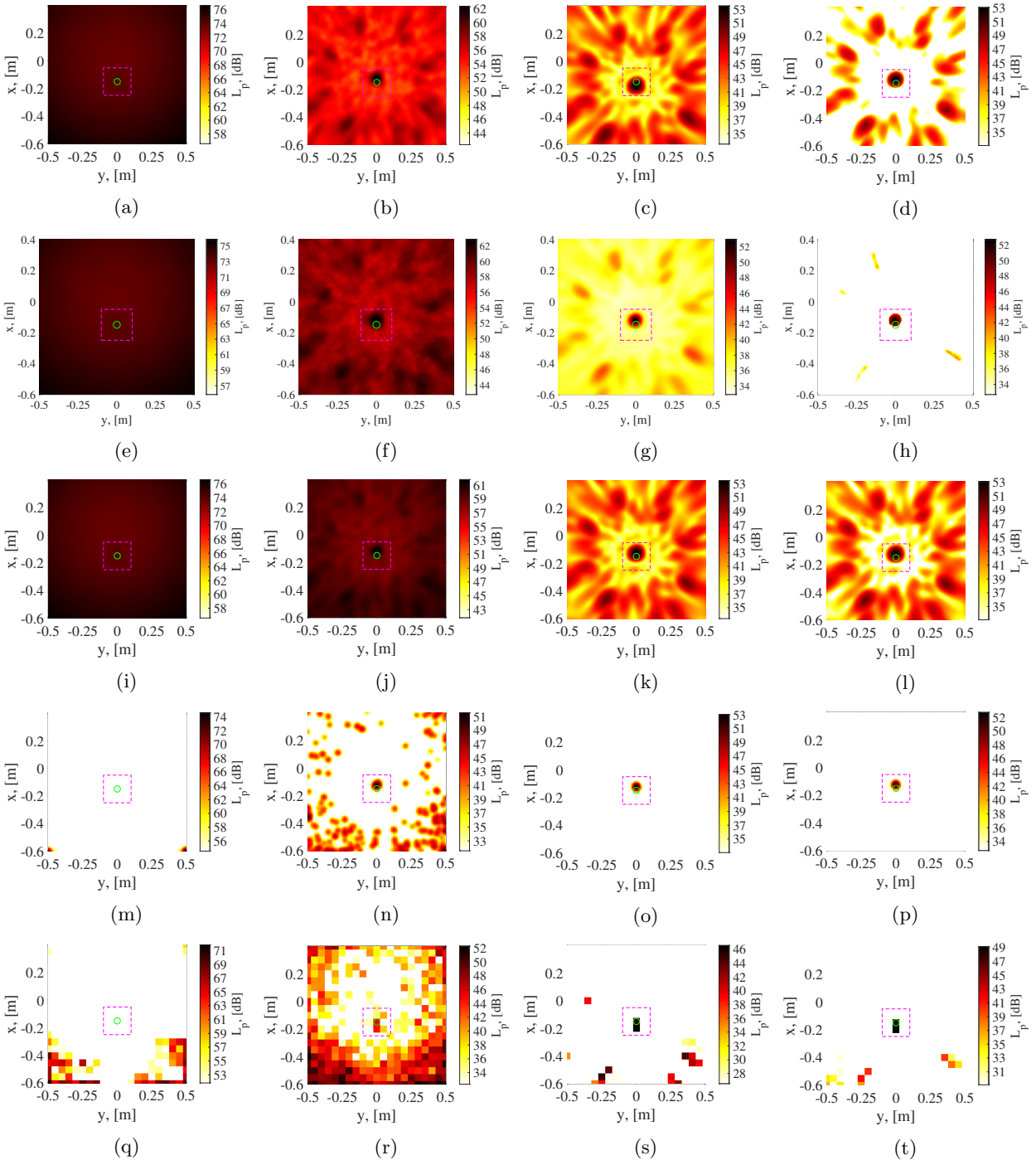

Figure 6: Acoustic source maps for the single speaker for $U_\infty = 34$ m/s and a one–third–octave frequency band centered at 10 kHz. The first two columns correspond to results obtained by the flush–mounted array without DR (first column) and with DR (second column) whereas the last two columns correspond to results obtained by the cavity array without DR (third column) and with DR (fourth column). The rows correspond to for: CFDBF (a–d), FUNBF (e–h), OB (i–l), CLEAN–SC (m–p), and DAMAS (q–t). The dashed magenta squares denote the ROI and the green circle denotes the speaker baffle.

800 Hz. Increasing the flow velocity to 34 m/s (Fig. 7d) reduces the effective source detection frequency range to frequencies higher than 3150 Hz for all methods. This range can, once again, be extended by the application of DR.

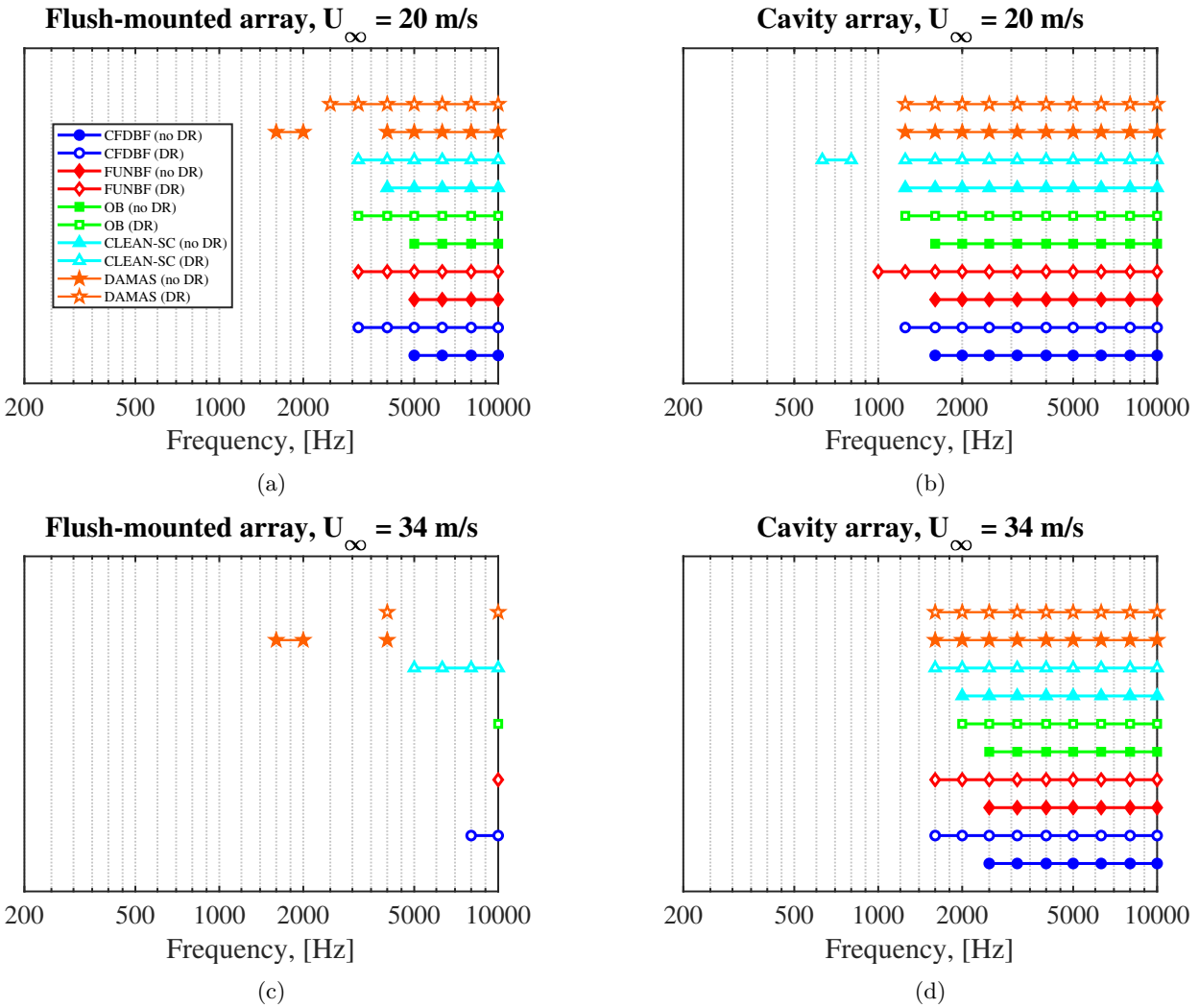

Figure 7: One–third–octave frequency bands for which the speaker was clearly detected in the acoustic source maps for: (a) Flush–mounted array with $U_\infty = 20$ m/s, (b) Flush–mounted array with $U_\infty = 20$ m/s, (c) Cavity array with $U_\infty = 34$ m/s, and (d) Cavity array with $U_\infty = 34$ m/s

IV.A.2. Frequency spectra

In terms of quantification of the emitted noise levels, the relative errors made by each method with respect to the frequency spectra reference solutions without flow (see solid lines in Fig. 3a) are evaluated as $\Delta L_\mathrm{p} = L_\mathrm{p,method} - L_\mathrm{p,ref}$. With this criterion $\Delta L_\mathrm{p} > 0$ corresponds to an overestimation, and vice versa. The absolute error averaged over the whole frequency range considered (the eleven one–third–octave bands between 1 kHz and 10 kHz) $\varepsilon = \overline{|\Delta L_\mathrm{p}|}$, i.e., the average $\mathcal{L}^1$ norm of the differences. The ε values for each method are depicted in the legends of Figs. 8 and 9.

Figure 8 presents the relative errors made by each acoustic imaging method for the flush–mounted array and for each case: the two flow velocities $U_\infty = 20$ m/s and 34 m/s combined with the application or not of DR. Some methods like DAMAS, OB, and especially CLEAN–SC have difficulties for providing estimates at the lower frequency bands and, for the worst–case scenario ($U_\infty = 34$ m/s and no DR, see Fig. 8c) also for some of the higher frequency bands. In fact, CLEAN–SC does not provide any spectrum at all, since no sound source is detected within the ROI for any frequency band.

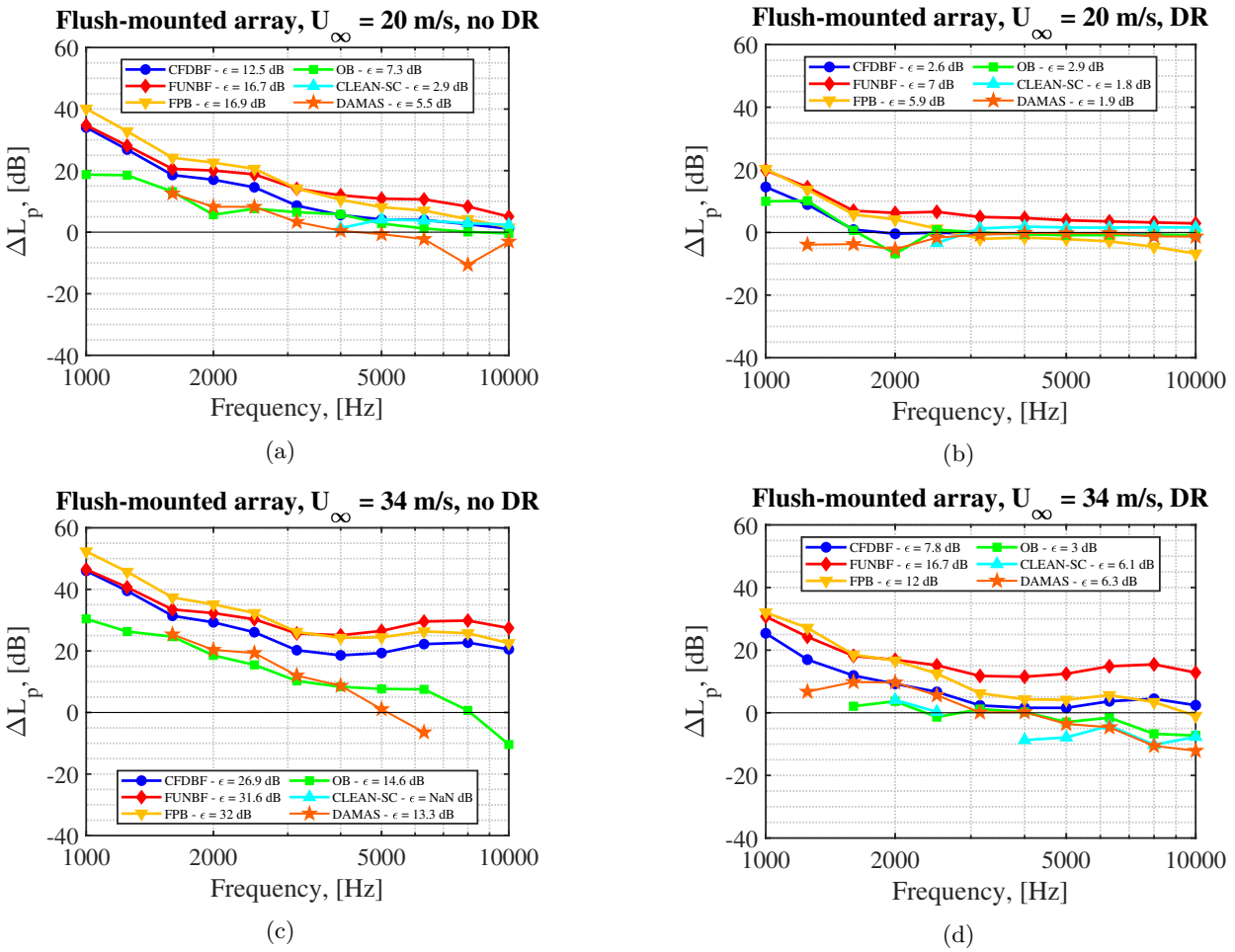

Figure 8: Relative errors made by each acoustic imaging method for the quantification of the sound emissions of the single speaker for the flush–mounted array for: (a) $U_\infty = 20$ m/s without DR, (b) $U_\infty = 20$ m/s with DR, (c) $U_\infty = 34$ m/s without DR, and (d) $U_\infty = 34$ m/s with DR.

As could be expected by the lower SNR, increasing the flow velocity leads to considerably higher average errors (up to 15 dB higher in some cases) in general, especially for the cases without DR. On the other hand, applying DR seems to reduce the overall errors made by all methods (up to almost 20 dB lower in some cases).

In terms of quantification accuracy, DAMAS and OB present the lowest errors, followed by CFDBF. CLEAN–SC provides relatively accurate estimates for the higher frequencies but does not detect the source for certain frequency bands. In general, the integration method FPB provides more accurate estimates than simply integrating the FUNBF source maps using the SPI approach.

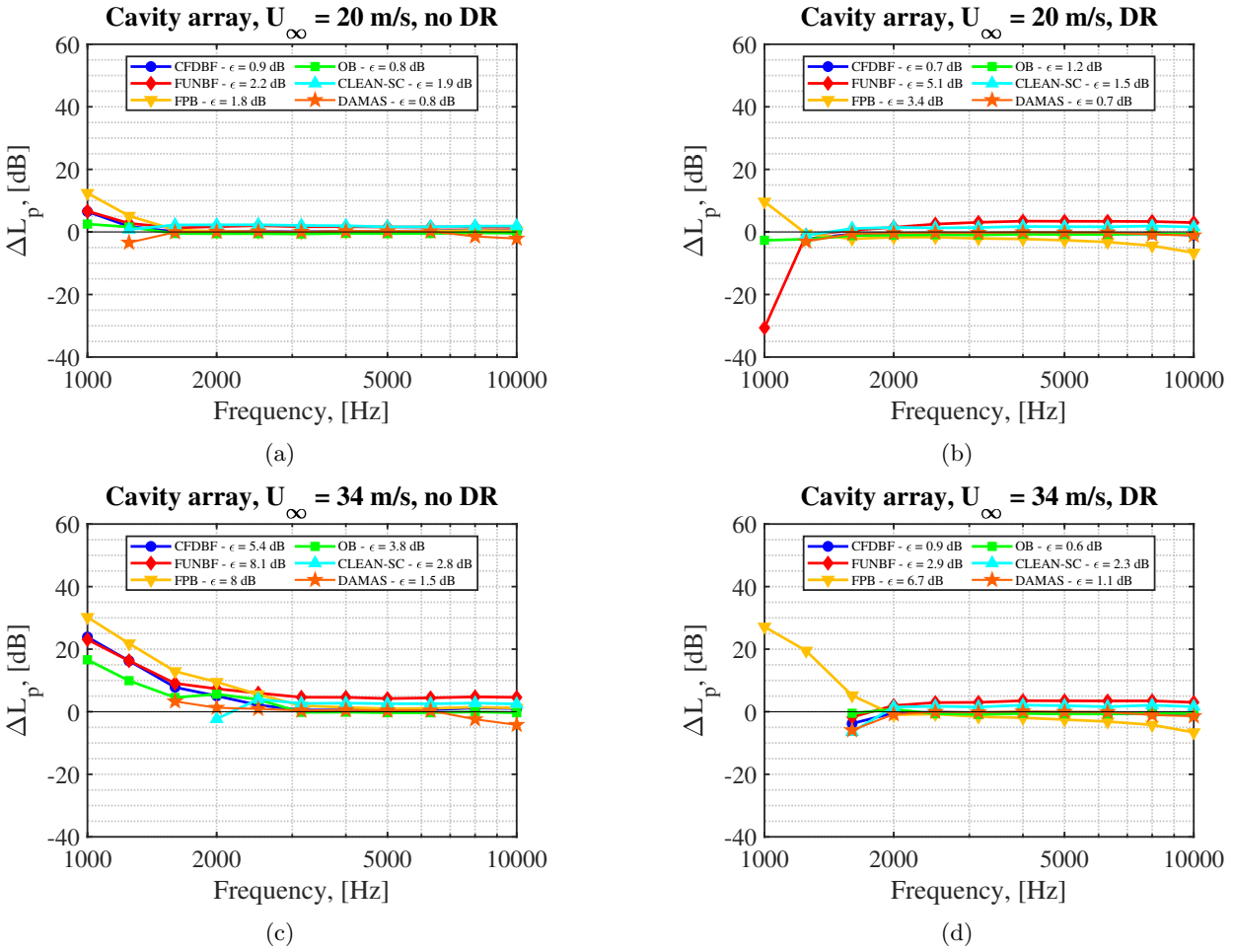

Figure 9: Relative errors made by each acoustic imaging method for the quantification of the sound emissions of the single speaker for the cavity array for: (a) $U_\infty = 20$ m/s without DR, (b) $U_\infty = 20$ m/s with DR, (c) $U_\infty = 34$ m/s without DR, and (d) $U_\infty = 34$ m/s with DR.

The quantitative errors made by the array with the microphones recessed within cavities (Fig. 9) are remarkably lower (up to even 20 dB lower in some cases) than those of the flush–mounted array from Fig. 8. Once again, DAMAS, OB, and CFDBF provide the most accurate estimations, with $\varepsilon < 1.5$ dB in most cases, although DAMAS does not detect the source for certain frequency bands. Interestingly, most methods (except for FPB) fail to detect the speaker for the case with $U_\infty = 34$ m/s with DR (Fig. 9d) at the lowest two frequency bands (1000 Hz and 1250 Hz), most likely due to the application of DR, which, depending on the eigenvalue distribution of the CSM, may provide negative (and hence non–physical) autopowers in certain grid points [14] that were neglected in the current study. Once again FPB provides more accurate estimates FUNBF.

Overall, for both arrays, lower frequencies show higher errors due to the lower SNR at those frequency bands, see Fig. 3b.

IV.B. Flat plate

IV.B.1. Acoustic source maps

Similar to the speaker case from section IV.A, Figures 10 and 11 present some exemplary acoustic source maps obtained by all the acoustic imaging methods considered and both array configurations and with and without DR applied. For each source map, the dashed magenta square represents the ROI and the green lines denote the flat plate and support plates

Figure 10 depicts the source maps for the case with $U_\infty = 20$ m/s and a one–third–octave frequency band centered at 2 kHz, which corresponds, respectively, to SNR values of 1.8 dB and 9.5 dB for the flush–mounted array and the one with the microphones recessed in cavities. For the flush–mounted array (first two columns), despite the lower flow velocity compared to the speaker examples from Figs. 5 and 6, none of the acoustic imaging methods manages to properly detect the expected distributed noise source along the trailing edge of the flat plate. Applying DR does not improve the results either, and all methods provide source distributions that are dominant along the top side of the selected scan grid ($x = 0.7$ m). On the other hand, the cavity array improves the source maps and, especially when DR is applied (last column), CFDBF (Fig. 10d) and FUNBF (Fig. 10h) manage to detect a distributed line source along the trailing edge of the flat plate (the expected result), as well as the sound reflections behind both vertical support plates. OB provides similar results but with the application of DR does not clean the source map as well as in the previous two examples (Fig. 10l). CLEAN–SC and DAMAS still localize most noise sources along the perimeter of the scan grid selected, but both CLEAN–SC with DR (Fig. 10p) and both cases of DAMAS (Fig. 10s and t) detect a relatively weaker source within the chosen ROI covering the trailing edge of the flat plate. This does not match with the expected physical noise generation mechanism, but both deconvolution methods are known for rendering distributed sound sources as point sources [45, 58].

The acoustic source maps for the case with $U_\infty = 34$ m/s and a one–third–octave frequency band centered at 4 kHz are presented in Fig. 11. This case corresponds to slightly lower SNR values of 0.5 dB and 9.2 dB for the flush–mounted array and the one with the microphones recessed in cavities, respectively. The noise source distributions observed are similar to those from Fig. 10: the flush–mounted array fails to detect the trailing–edge noise source, and only CFDBF, FUNBF, and OB render a distributed noise source, which is more slender due to the higher frequency. In this case, CLEAN–SC and DAMAS do not detect any major noise sources within the ROI.

IV.B.2. Frequency spectra

In contrast with the single speaker case from section IV.A, the actual noise emissions of the trailing edge of the flat plate are not known precisely, and, therefore, it is more challenging to have reference spectra to evaluate the accuracy of the estimations obtained by the acoustic imaging methods. Hence, the estimations of the Brooks, Pope, and Marcolini (BPM) semi–empirical noise prediction model [71] are employed as a reference. The model predicts the TBL trailing–edge noise and vortex shedding noise contributions, among others. The agreement of the results of the acoustic imaging methods with the predictions of this model is evaluated in Figs. 12 and 13 for the flush–mounted array and the cavity array, respectively. However, as with every semi–empirical prediction tool, the accuracy of the BPM model is not perfect, so these comparisons are considered indicative.

It can be observed that for the flush–mounted array without applying DR (Fig. 12a and c), only CFDBF, FUNBF, and FPB provide continuous estimations for the spectra for both flow velocities, but considerably higher than the estimations of the BPM model. CLEAN–SC, DAMAS, and OB do not provide any spectral estimations when DR is not applied. For the cases with DR (Fig. 12b and d), the estimated spectra are considerably lower and, hence, closer to the BPM estimations. For the case with $U_\infty = 20$ m/s (Fig. 12b), CFDBF provides a relatively good agreement with the BPM model for frequencies below 2 kHz, and for the case with $U_\infty = 34$ m/s (Fig. 12d), DAMAS matches the model predictions well for 1 kHz and between the frequency bands 1600 Hz and 3150 Hz but does not provide any estimate outside of that range. In general, none of the methods is able to provide accurate estimations for the flush–mounted array. CLEAN–SC does not function well for this case and OB only manages to provide discrete quantitative estimates below 5 kHz, although relatively close to those from the BPM model.

In general, the estimated spectra for the cavity array case (Fig. 13) are considerably closer to those by the BPM model, basically, because the average microphone signals (represented as solid black lines) are considerably lower than those for the flush–mounted array. Even the results of CFDBF and FUNBF without

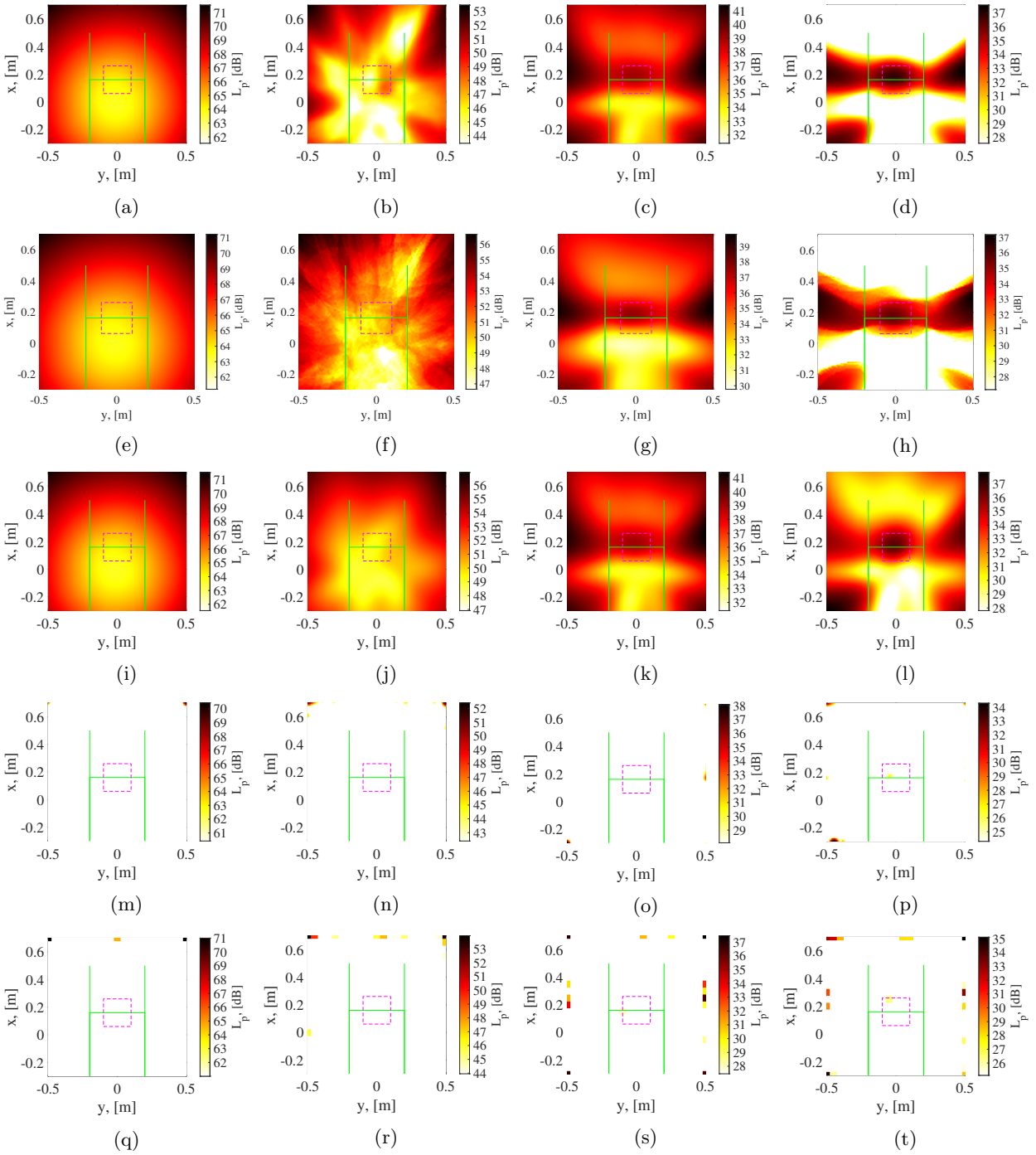

Figure 10: Acoustic source maps for the flat plate for $U_\infty = 20$ m/s and a one–third–octave frequency band centered at 2 kHz. The first two columns correspond to results obtained by the flush–mounted array without DR (first column) and with DR (second column) whereas the last two columns correspond to results obtained by the cavity array without DR (third column) and with DR (fourth column). The rows correspond to for: CFDBF (a–d), FUNBF (e–h), OB (i–l), CLEAN–SC (m–p), and DAMAS (q–t). The dashed magenta squares denote the ROI and the green lines denote the flat plate and support plates.

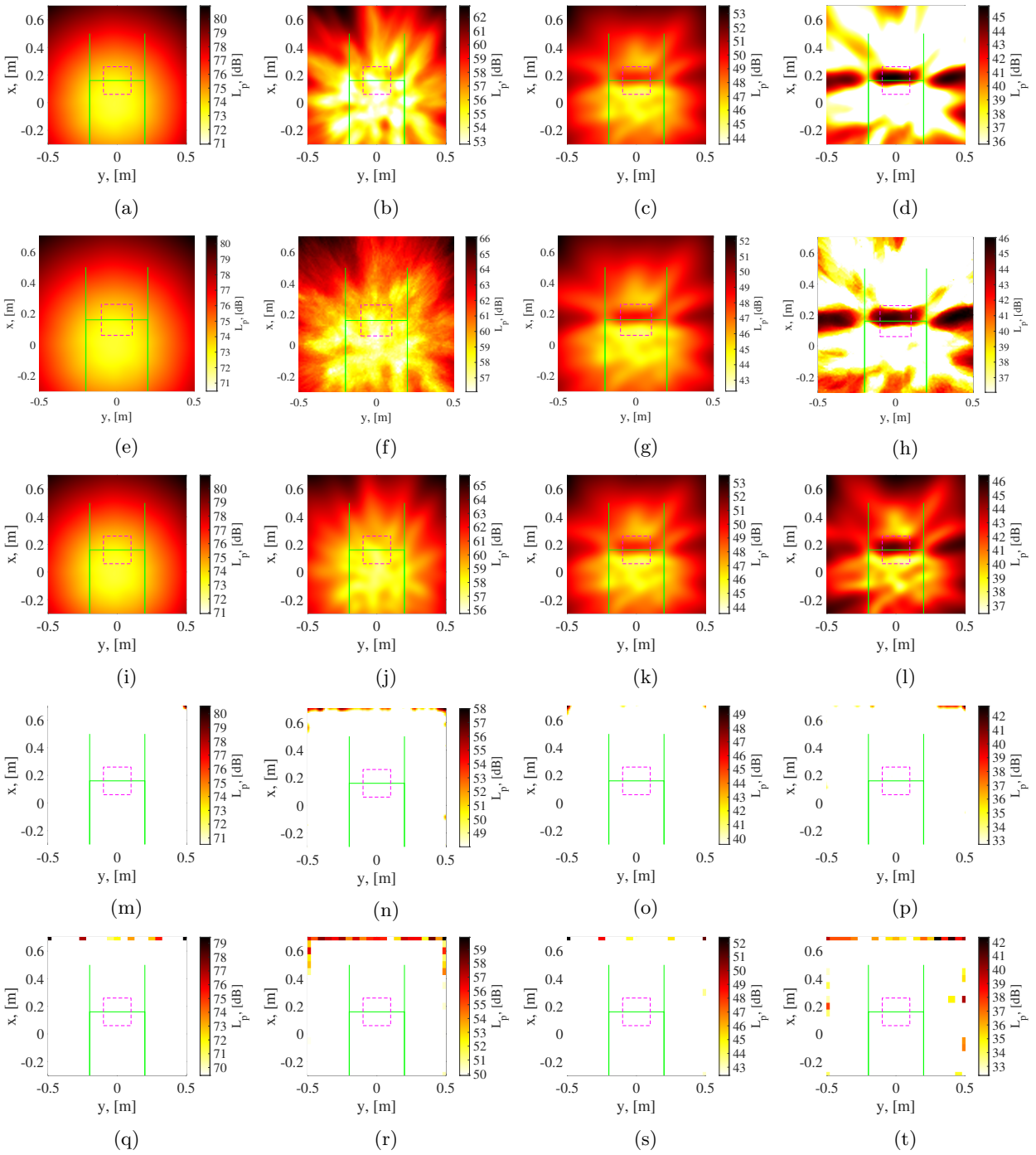

Figure 11: Acoustic source maps for the flat plate for $U_\infty = 34$ m/s and a one–third–octave frequency band centered at 4 kHz. The first two columns correspond to results obtained by the flush–mounted array without DR (first column) and with DR (second column) whereas the last two columns correspond to results obtained by the cavity array without DR (third column) and with DR (fourth column). The rows correspond to for: CFDBF (a–d), FUNBF (e–h), OB (i–l), CLEAN–SC (m–p), and DAMAS (q–t). The dashed magenta squares denote the ROI and the green lines denote the flat plate and support plates.

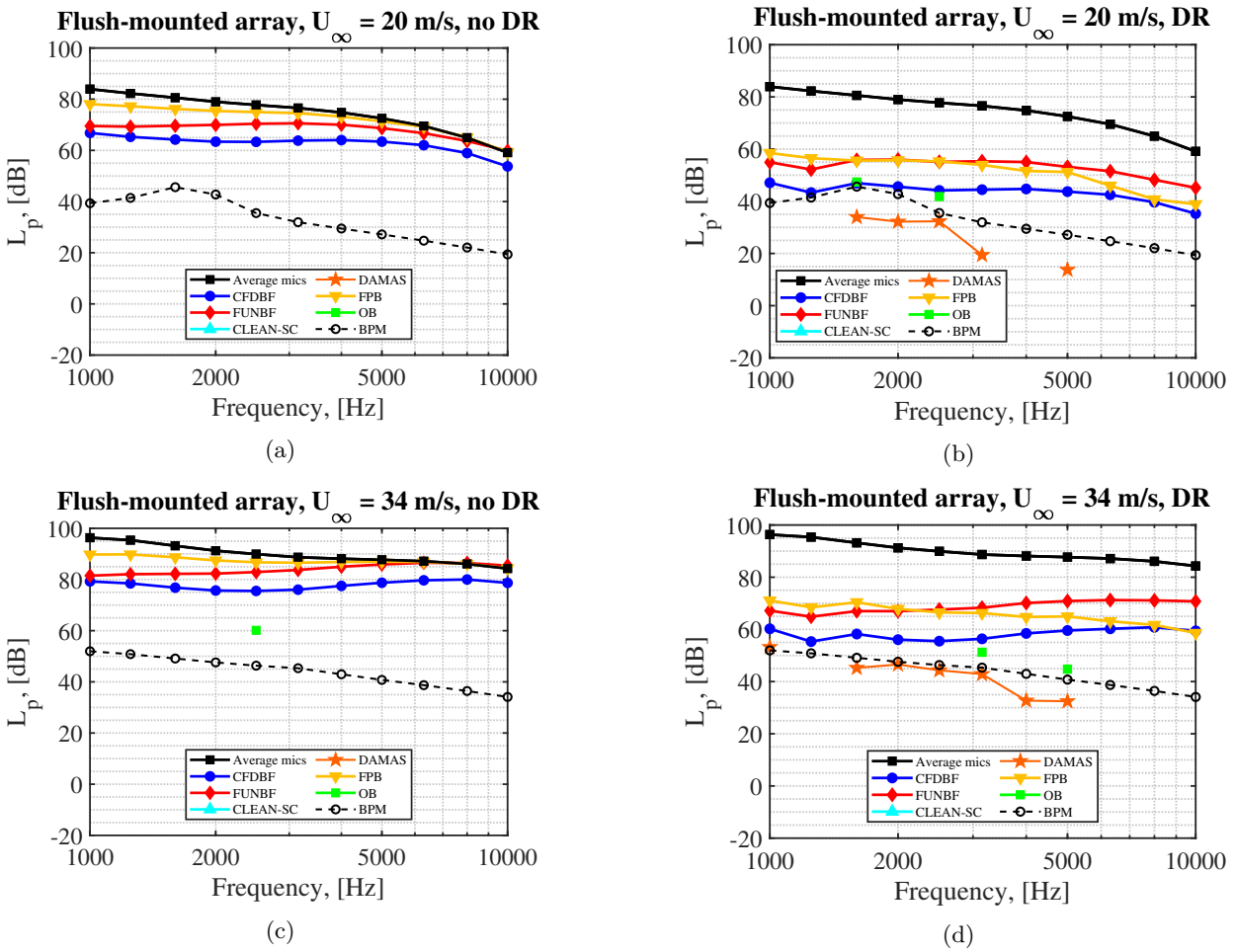

Figure 12: Integrated frequency spectra within the selected ROI estimated by each acoustic imaging method for the quantification of the sound emissions of the trailing edge of the flat plate for the flush–mounted array for: (a) $U_\infty = 20$ m/s without DR, (b) $U_\infty = 20$ m/s with DR, (c) $U_\infty = 34$ m/s without DR, and (d) $U_\infty = 34$ m/s with DR. In all figures, the BPM estimations and the average microphone response for the array are also depicted for reference.

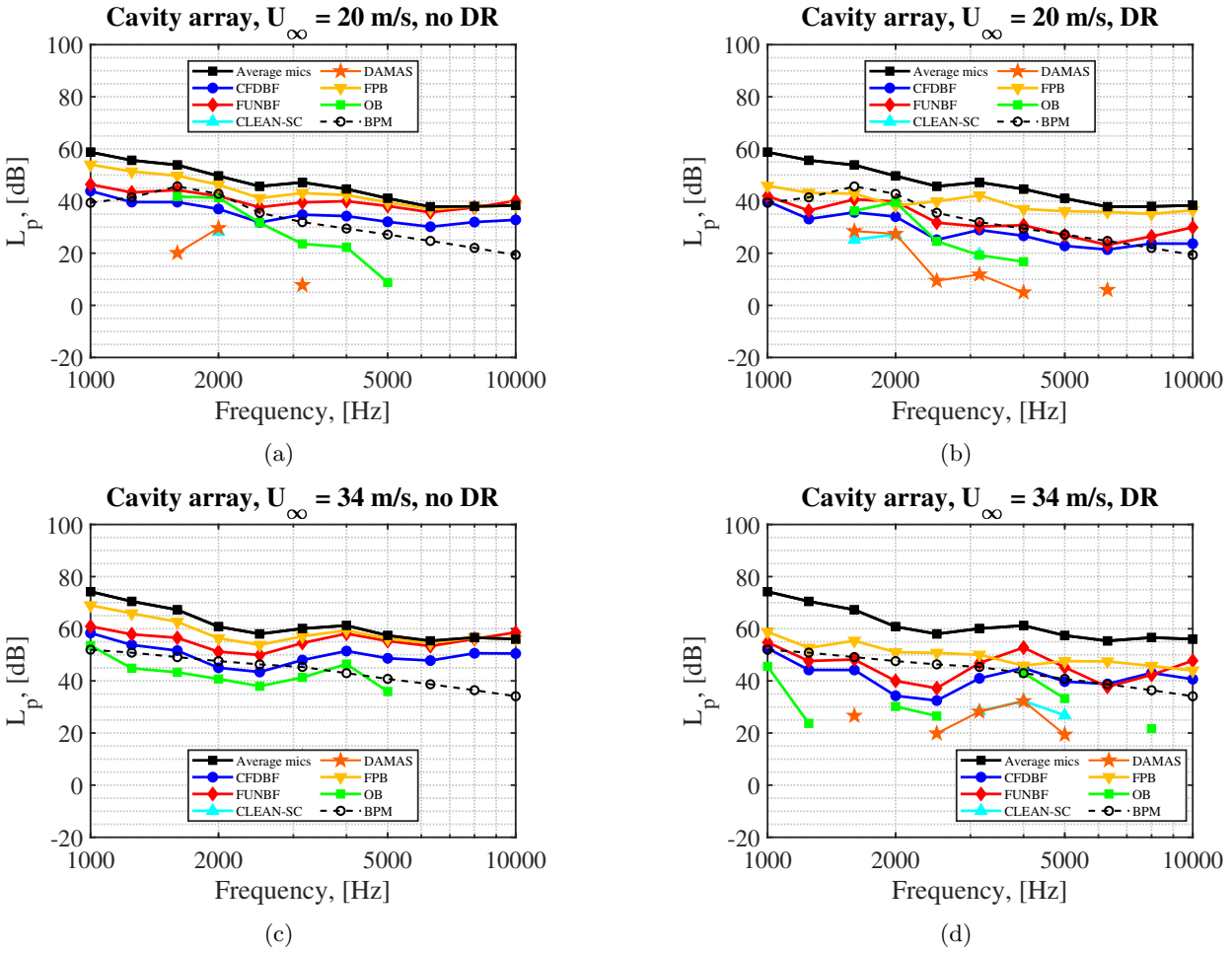

Figure 13: Integrated frequency spectra within the selected ROI estimated by each acoustic imaging method for the quantification of the sound emissions of the trailing edge of the flat plate for the flush–mounted array for: (a) $U_\infty = 20$ m/s without DR, (b) $U_\infty = 20$ m/s with DR, (c) $U_\infty = 34$ m/s without DR, and (d) $U_\infty = 34$ m/s with DR. In all figures, the BPM estimations and the average microphone response for the array are also depicted for reference.

applying DR (Figs. 13a and c) present a relatively close agreement to the model estimations, especially below 3150 Hz. Once again, DAMAS and CLEAN–SC have difficulties providing continuous quantitative estimations, but OB seems to overcome that issue to some extent and offers similar results as those by CFDBF and FUNBF for a large part of the frequency range considered. In this case, FPB provides consistently higher values than FUNBF. Applying DR to the CSM (Figs. 13b and d) reduces the levels in the estimated spectra to some extent, but less remarkably than for the flush–mounted array (Fig. 12. The application of DR does seem to help DAMAS and CLEAN–SC to provide estimates for more frequency bands than for the cases without. In general, for all the four cases shown in Fig. 13, the estimations at higher frequencies present a worse agreement with the BPM model predictions, despite having a higher SNR in these bands. This difference is mitigated to some extent by the application of DR. All in all, CFDBF and FUNBF seem to provide the closest agreement to the predictions by the BPM model, especially for the case with $U_\infty = 20$ m/s and DR (Fig. 13b).

V. Conclusions and outlook

This paper investigated the performance of several advanced acoustic imaging techniques for performing aeroacoustic measurements with microphone arrays in closed–section wind tunnels. Two different experimental setups were considered: a flush–mounted array on the wind tunnel wall (considered as a baseline) and an array with its microphones recessed in cavities and covered with an acoustically transparent covering in order to mitigate the TBL pressure fluctuations.

The acoustic imaging methods considered were CFDBF, FUNBF (and FPB for the integration of the maps obtained), OB, CLEAN–SC, and DAMAS. Two different test cases were considered: a single speaker (outside of the flow) emitting broadband sound as a reference signal simulating a point source, and a flat plate inside of the flow with an expected distributed noise source along its trailing edge.

In general, the array with microphones recessed in cavities benefited from considerably higher signal–to–noise ratios and, hence, managed to provide clearer source maps and more accurate quantitative estimates. Such cavities can be easily implemented in already existing closed–wall wind tunnels more easily compared to a full refurbishment to convert the whole facility to a hybrid wind tunnel. Removing the main diagonal of the cross–spectral matrix additionally helps to improve the results further.

In general, DAMAS and OB were determined to be the best performing methods for the case with a single speaker (point source) when considering source localization and quantification. On the other hand, CFDBF and FUNBF were the most suitable methods for the more practical case with the flat plate (trailing edge as distributed sound source), whereas the other techniques fail to properly identify it.

Future work may include larger microphone arrays, higher flow velocities, and different microphone cavity geometries to investigate how the findings from this paper hold to those conditions. Additionally, the potential improvement provided by the cavities and advanced acoustic imaging methods for three–dimensional acoustic source mapping in closed–section wind tunnels, such as experiments combining asynchronous microphone array measurements from different points of view [72], should also be evaluated.

Acknowledgements

The experimental campaign employed in this paper is part of the research programme THAMES with project number 15215, which is (partly) financed by the Dutch Research Council (NWO). The authors would also like to acknowledge the THAMES project partners for their insight and assistance.

References

[1] Snellen, M., Merino-Martinez, R., and Simons, D. G., "Assessment of noise level variability on landing aircraft using a phased microphone array," *Journal of Aircraft*, Vol. 54, No. 6, 2017, pp. 2173–2183.

[2] Merino-Martinez, R., Vieira, A., Snellen, M., and Simons, D. G., "Sound quality metrics applied to aircraft components under operational conditions using a microphone array," 25^{th} *AIAA/CEAS Aeroacoustics Conference, May 20 – 24 2019, Delft, The Netherlands*, 2019, AIAA paper 2019–2513.

[3] Michel, U. and Barsikow, B., "Localisation of sound sources on moving vehicles with microphone arrays,"

Proceedings of EuroNoise 2003, May 19 – 21 2003, Naples, Italy, No. paper ID 537, 2003.

[4] Oerlemans, S., Sijtsma, P., and Méndez López, B., "Location and Quantification of Noise Sources on a Wind Turbine," *Journal of Sound and Vibration*, Vol. 299, 2007, pp. 869–883.

[5] Merino-Martinez, R., Pieren, R., and Schäffer, B., "Holistic approach to wind turbine noise: From blade trailing–edge modifications to annoyance estimation," *Renewable and Sustainable Energy Reviews*, Vol. 148, No. 111285, May 2021, pp. 1–14.

[6] Merino-Martinez, R., Heblij, S. J., Bergmans, D. H. T., Snellen, M., and Simons, D. G., "Improving Aircraft Noise Predictions by Considering the Fan Rotational Speed," *Journal of Aircraft*, Vol. 56, No. 1, 2019, pp. 284–294.

[7] Mueller, T., *Aeroacoustic Measurements*, Springer Science & Business Media, Berlin, Germany, 2002, ISBN: 978–3–642–07514–8.

[8] Stoker, R., Guo, Y., Streett, C., and Burnside, N., "Airframe noise source locations of a 777 aircraft in flight and comparisons with past model–scale tests," 9^{th} *AIAA/CEAS Aeroacoustics Conference, May 12 – 14 2003, Hilton Head, South California, USA*, 2003, AIAA paper 2003–3232.

[9] Pereira Gomes, J., Bergmann, A., and Holthusen, H., "Aeroacoustic wind tunnel design (part of the Aircraft Noise Generation and Assessment special issue)," *CEAS Aeronautical Journal*, Vol. 10, No. 1, March 2019, pp. 231–249, DOI: 10.1007/s13272-019-00372-7.

[10] Merino-Martinez, R., Neri, E., Snellen, M., Kennedy, J., Simons, D. G., and Bennett, G. J., "Analysis of nose landing gear noise comparing numerical computations, prediction models and flyover and wind–tunnel measurements," 24^{th} *AIAA/CEAS Aeroacoustics Conference, June 25 – 29 2018, Atlanta, Georgia, USA*, 2018, AIAA paper 2018–3299.

[11] Spehr, C. and Ahlefeldt, T., "Comparison of Microphone Array Measurements in the Closed Test Section of LSWT and ETW (part of the Aircraft Noise Generation and Assessment special issue)," *CEAS Aeronautical Journal*, Vol. 10, 2019, pp. 267–285.

[12] Sijtsma, P., "Phased array beamforming applied to wind tunnel and fly–over tests," Tech. Rep. NLR–TP–2010–549, National Aerospace Laboratory (NLR), Anthony Fokkerweg 2, 1059 CM Amsterdam, P.O. Box 90502, 1006 BM Amsterdam, The Netherlands, December 2010.

[13] Merino-Martinez, R., *Microphone arrays for imaging of aerospace noise sources*, Ph.D. thesis, Delft University of Technology, 2018, ISBN: 978–94–028–1301–2.

[14] Merino-Martinez, R., Sijtsma, P., Snellen, M., Ahlefeldt, T., Antoni, J., Bahr, C. J., Blacodon, D., Ernst, D., Finez, A., Funke, S., Geyer, T. F., Haxter, S., Herold, G., Huang, X., Humphreys, W. M., Leclère, Q., Malgoezar, A., Michel, U., Padois, T., Pereira, A., Picard, C., Sarradj, E., Siller, H., Simons, D. G., and Spehr, C., "A review of acoustic imaging methods using phased microphone arrays (part of the Aircraft Noise Generation and Assessment special issue)," *CEAS Aeronautical Journal*, Vol. 10, No. 1, March 2019, pp. 197–230.

[15] Bahr, C. J. and Horne, W. C., "Subspace–based background noise subtraction applied to aeroacoustic wind tunnel testing," *International Journal of Aeroacoustics*, Vol. 16, No. 4–5, 2017, pp. 299–325, SAGE Publications Ltd. London, United Kingdom.

[16] VanDercreek, C. P., Merino-Martinez, R., Snellen, M., and Simons, D. G., "Comparison of cavity geometries for a microphone array in a open–jet wind–tunnel experiment," 8^{th} *Berlin Beamforming Conference, March 2 – 3 2020, Berlin, Germany*, GFaI, e.V., Berlin, 2020, BeBeC–2020–D7.

[17] Arce León, C., Merino-Martinez, R., Ragni, D., Avallone, F., and Snellen, M., "Boundary layer characterization and acoustic measurements of flow–aligned trailing edge serrations," *Experiments in Fluids*, Vol. 57, No. 182, October 2016, pp. 1 – 22.

[18] Rubio Carpio, A., Merino-Martinez, R., Avallone, F., Ragni, D., Snellen, M., and van der Zwaag, S., "Experimental characterization of the turbulent boundary layer over a porous trailing edge for noise abatement," *Journal of Sound and Vibration*, Vol. 443, March 2019, pp. 537–558.

[19] Merino-Martinez, R., Kennedy, J., and Bennett, G. J., "Experimental study of realisitic low–noise technologies applied to a full-scale nose landing gear," *Aerospace Science and Technology*, Vol. 113, No. 106705, June 2021, pp. 1–20.

[20] Pagani, C. C. J., Souza, D. S., and Medeiros, M. A. F., "Slat Noise: Aeroacoustic Beamforming in Closed–Section Wind Tunnel with Numerical Comparison," *AIAA Journal*, Vol. 54, No. 7, April 2016, pp. 2100–2115.

[21] Jaeger, S. M., Horne, W., and Allen, C., "Effect of surface treatment on array microphone self–noise," 6^{th} *AIAA/CEAS Aeroacoustics Conference, June 12–14 2016, Lahaina, HI, USA*, 2000, AIAA paper 2000-1937.

[22] Fleury, V., Coste, L., Davy, R., and Mignosi, A., "Optimization of Microphone Array Wall-Mountings in Closed-Section Wind Tunnels," 16^{th} *AIAA/CEAS Aeroacoustics Conference, Stockholm, Sweden*, 2010, AIAA paper 2010–3738.

[23] Sinnige, T., Della Corte, B., de Vries, R., Avallone, F., Merino-Martinez, R., Ragni, D., Eitelberg, G., and Veldhuis, L. L. M., "Alleviation of Propeller–Slipstream–Induced Unsteady Pylon Loading by a Flow–Permeable Leading Edge," *Journal of Aircraft*, Vol. 56, No. 3, May–June 2019, pp. 1214–1230, DOI: 10.2514/1.C035250.

[24] VanDercreek, C. P., Merino-Martinez, R., Sijtsma, P., and Snellen, M., "Evaluation of the effect of microphone cavity geometries on acoustic imaging in wind tunnels," *Applied Acoustics*, Vol. 181, No. 108154, April 2021, pp. 1–15.

[25] Duell, E., Walter, J., Arnette, S., and J., Y., "Recent Advances in Large–Scale Aeroacoustic Wind Tunnels," 8^{th} *AIAA/CEAS Aeroacoustics Conference, 17 – 19 June 2002, Breckenridge, Co, USA*, 2002, AIAA paper 2002–2503.

[26] Guidati, S., Brauer, C., and Wagner, S., "The reflection canceller – Phased array measurements in a reverberating environment," 8^{th} *AIAA/CEAS Aeroacoustics Conference and Exhibit, June 17 – 19, 2002, Breckenridge, Colorado, USA*, 2002, AIAA paper 2002–2462.

[27] Sijtsma, P. and Holthusen, H., "Corrections for Mirror Sources in Phased Array Processing Techniques," 9^{th} *AIAA/CEAS Aeroacoustics Conference, May 12 – 14, 2003, Hilton Head, South Carolina, USA*, 2003, AIAA paper 2003–3196.

[28] Merino-Martinez, R., Rubio Carpio, A., Lima Pereira, L. T., van Herk, S., Avallone, F., Kotsonis, M., and Ragni, D., "Aeroacoustic design and characterization of the 3D–printed, open–jet, anechoic wind tunnel of Delft University of Technology," *Applied Acoustics*, Vol. 170, No. 107504, June 2020, pp. 1–16.

[29] Anderson, J. D. J., *Fundamentals of Aerodynamics*, McGraw–Hill Series in Aeronautical and Aerospace Engineering, Third ed., 2001, ISBN: 0–07–237335–0.

[30] Padois, T., Prax, C., and Valeau, V., "Numerical validation of shear flow corrections for beamforming acoustic source localisation in open wind–tunnels," *Applied Acoustics*, Vol. 74, 2013, pp. 591–601.

[31] Amiet, R. K., "Refraction of sound by a shear layer," *Journal of Sound and Vibration*, Vol. 58, No. 4, 1978, pp. 467–482.

[32] Ernst, D., Spehr, C., and Berkefeld, T., "Decorrelation of Acoustic Wave Propagation through the Shear Layer in Open Jet Wind Tunnel," 21^{st} *AIAA/CEAS Aeroacoustics Conference, June 22 – 26 2015, Dallas, TX, USA*, 2015, AIAA paper 2015–2976.

[33] Sijtsma, P., Oerlemans, S., Tibbe, T., Berkefeld, T., and Spehr, C., "Spectral broadening by shear layers of open jet wind tunnels," 20^{th} *AIAA/CEAS Aeroacoustics Conference, June 16 – 20 2014, Atlanta, GA, USA*, 2014, AIAA paper 2014–3178.

[34] Merino-Martinez, R., van der Velden, W. C. P., Avallone, F., and Ragni, D., "Acoustic measurements of a DU96–W–180 airfoil with flow–misaligned serrations at a high Reynolds number in a closed–section wind tunnel," 7^{th} *International Meeting on Wind Turbine Noise, May 2 – 5 2017, Rotterdam, the Netherlands*, International Institute of Noise Control Engineering (I-INCE), 1A/B Westminster Chambers, 106 Lord Street, Southport PR8 1LF, United Kingdom, 2017.

[35] Smith, B. S., Camargo, H. E., Burdisso, R. A., and Devenport, W. J., "Development of a Novel Acoustic Wind Tunnel Concept," 11^{th} *AIAA/CEAS Aeroacoustics Conference, May 23 – 25 2005, Monterey, California, USA*, 2005, AIAA paper 2005–3053.

[36] Remillieux, M. C., Crede, E. D., Camargo, H. E., Burdisso, R. A., J., D. W., Rasnick, M., van Seeters, P., and Chou, A., "Calibration and Demonstration of the New Virginia Tech Anechoic Wind Tunnel," 14^{th} *AIAA/CEAS Aeroacoustics Conference (*29^{th} *AIAA Aeroacoustics Conference), May 5–7, 2008, Vancouver, British Columbia, Canada*, 2008, AIAA paper 2008–2911.

[37] Sanders, M. P. J., Koenjer, C. F. J., Botero-Bolivar, L., dos Santos F. L., Venner, C. H., and de Santana, L. D., "Trailing–Edge Noise Comparability in Open, Closed, and Hybrid Wind Tunnel Test Sections," *AIAA Journal*, Vol. TBD, No. TBD, 2022, pp. TBD.

[38] Kröber, S., *Comparability of Microphone Array Measurements in Open and Closed Wind Tunnels*, Ph.D. thesis, Technical University of Berlin, 2014.

[39] Koop, L. and Ehrenfried, K., "Microphone–array processing for wind–tunnel measurements with strong background noise," 14^{th} *AIAA/CEAS Aeroacoustics Conference (*29^{th} *AIAA Aeroacoustics Conference), May 5–7, 2008, Vancouver, British Columbia, Canada*, 2008, AIAA paper 2008–2907.

[40] Blacodon, D., "Array Processing for Noisy Data: Application for Open and Closed Wind Tunnels," *AIAA Journal*, Vol. 49, No. 1, 2011, pp. 55–66.

[41] Blacodon, D. and Bulté, J., "Reverberation cancellation in a closed test section of a wind tunnel using a multi-microphone cepstral method," *Journal of Sound and Vibration*, Vol. 333, 2014, pp. 26–34.

[42] Leclère, Q., Pereira, A., Bailly, C., Antoni, J., and Picard, C., "A unified formalism for acoustic imaging based on microphone array measurements," *International Journal of Aeroacoustics*, Vol. 16, No. 4–5, 2017, pp. 431–456, SAGE Publications Ltd. London, United Kingdom.

[43] Sarradj, E., Herold, G., Sijtsma, P., Merino-Martinez, R., Malgoezar, A. M. N., Snellen, M., Geyer, T. F., Bahr, C. J., Porteous, R., Moreau, D. J., and Doolan, C. J., "A microphone array method benchmarking exercise using synthesized input data," 23^{rd} *AIAA/CEAS Aeroacoustics Conference, June 5 – 9 2017, Denver, CO, USA*, 2017, AIAA paper 2017–3719.

[44] Bahr, C. J., Humphreys, W. M., Ernst, D., Ahlefeldt, T., Spehr, C., Pereira, A., Leclère, Q., Picard, C., Porteus, R., Moreau, D. J., Fischer, J., and Doolan, C. J., "A comparison of microphone phased array methods applied to the study of airframe noise in wind tunnel testing," 23^{rd} *AIAA/CEAS Aeroacoustics Conference, June 5 – 9 2017, Denver, CO, USA*, 2017, AIAA paper 2017–3718.

[45] Merino-Martinez, R., Luesutthiviboon, S., Zamponi, R., Rubio Carpio, A., Ragni, D., Sijtsma, P., Snellen, M., and Schram, C., "Assessment of the accuracy of microphone array methods for aeroacoustic measurements," *Journal of Sound and Vibration*, Vol. 470, No. 115176, January 2020, pp. 1–24.

[46] van Veen, B. D. and Buckley, K. M., "Beamforming: A Versatile Approach to Spatial Filtering," *IEEE ASSP Magazine*, Vol. 5, No. 2, April 1988, pp. 4–24.

[47] Lord Rayleigh, F. R. S., "XXXI. Investigations in Optics with special reference to the Spectroscope," *The London, Edinburgh and Dublin Philosophical Magazine and Journal of Science*, Vol. 8, No. 49, October 1879, pp. 261–274.

[48] Brooks, T. F. and Humphreys, W. M., "Effect of Directional Array Size on the Measurement of Airframe Noise Components," 5^{th} *AIAA/CEAS Aeroacoustics Conference. Bellevue, WA, USA*, 1999, AIAA paper 1999–1958.

[49] Merino-Martinez, R., Sijtsma, P., and Snellen, M., "Inverse Integration Method for Distributed Sound Sources," 7^{th} *Berlin Beamforming Conference, March 5 – 6 2018, Berlin, Germany*, GFaI, e.V., Berlin, 2018, BeBeC–2018–S07.

[50] Merino-Martinez, R., Sijtsma, P., Rubio Carpio, A., Zamponi, R., Luesutthiviboon, S., Malgoezar, A. M. N., Snellen, M., Schram, C., and Simons, D. G., "Integration methods for distributed sound sources," *International Journal of Aeroacoustics*, Vol. 18, No. 4–5, 2019, pp. 444–469.

[51] Dougherty, R. P., "Functional Beamforming," 5^{th} *Berlin Beamforming Conference, February 19 – 20 2014, Berlin, Germany*, GFaI, e.V., Berlin, 2014, BeBeC–2014–01.

[52] Merino-Martinez, R., Snellen, M., and Simons, D. G., "Functional beamforming applied to imaging of flyover noise on landing aircraft," *Journal of Aircraft*, Vol. 53, No. 6, November–December 2016, pp. 1830–1843.

[53] Merino-Martinez, R., Snellen, M., and Simons, D. G., "Functional Beamforming Applied to Full Scale Landing Aircraft," 6^{th} *Berlin Beamforming Conference, February 29 – March 1 2016, Berlin, Germany*, GFaI, e.V., Berlin, 2016, BeBeC–2016–D12.

[54] Merino-Martinez, R., Bertsch, L., Snellen, M., and Simons, D. G., "Analysis of landing gear noise during approach," 22^{nd} *AIAA/CEAS Aeroacoustics Conference, May 30 – June 1 2016, Lyon, France*, 2016, AIAA paper 2016–2769.

[55] Merino-Martinez, R. and Snellen, M., "Implementation of tonal cavity noise estimations in landing gear noise prediction models," 26^{th} *AIAA/CEAS Aeroacoustics Conference, June 15 – 19 2020, Virtual Event*, 2020, AIAA paper 2020–2578.

[56] Dougherty, R. P., "Determining Spectra of Aeroacoustic Sources from Microphone Array Data," 25^{th} *AIAA/CEAS Aeroacoustics Conference, May 20 – 23 2019, Delft, The Netherlands*, 2019, AIAA paper 2019–2745.

[57] Dougherty, R. P., "Adaptive Projection Beamforming," 8^{th} *Berlin Beamforming Conference, March 2 – 3 2020, Berlin, Germany*, GFaI, e.V., Berlin, 2020.

[58] Merino-Martinez, R., Herold, G., Snellen, M., and Dougherty, R. P., "Assessment and comparison of the performance of functional projection beamforming for aeroacoustic measurements," 8^{th} *Berlin Beamforming Conference, March 2 – 3 2020, Berlin, Germany*, GFaI, e.V., Berlin, 2020, BeBeC–2020–S7.

[59] Sarradj, E., "A fast signal subspace approach for the determination of absolute levels from phased microphone array measurements," *Journal of Sound and Vibration*, Vol. 329, No. 9, April 2010, pp. 1553–1569.

[60] Pillai, S. U., *Array Signal Processing*, Springer, 1989, ISBN: 978–3–540–96951–8.

[61] Sijtsma, P., "CLEAN based on spatial source coherence," *International Journal of Aeroacoustics*, Vol. 6, No. 4, 2007, pp. 357–374, SAGE Publications Ltd. London, United Kingdom.

[62] Luesutthiviboon, S., Malgoezar, A. M. N., Merino-Martinez, R., Snellen, M., Sijtsma, P., and Simons, D. G., "Enhanced HR–CLEAN–SC for resolving multiple closely spaced sound sources," *International Journal of Aeroacoustics*, Vol. 18, No. 4–5, 2019, pp. 392–413.

[63] Sijtsma, P., Merino-Martinez, R., Malgoezar, A. M. N., and Snellen, M., "High–Resolution CLEAN–SC: Theory and Experimental Validation," *International Journal of Aeroacoustics*, Vol. 16, No. 4–5, 2017, pp. 274–298, SAGE Publications Ltd. London, United Kingdom.

[64] Brooks, T. F. and Humphreys, W. M., "A Deconvolution Approach for the Mapping of Acoustic Sources (DAMAS) determined from phased microphone arrays," 10^{th} *AIAA/CEAS Aeroacoustics Conference, May 10 – 12 2004, Manchester, UK*, 2004, AIAA paper 2004–2954.

[65] G.R.A.S. Sound & Vibration – 40PH CCP Free–field array microphone, "http://www.gras.dk/products/special-microphone/array-microphones/product/178-40ph," Accessed in March 2017.

[66] Luesutthiviboon, S., Malgoezar, A., Snellen, M., Sijtsma, P., and Simons, D. G., "Improving Source Discrimination Performance by Using an Optimized Acoustic Array and Adaptive High–Resolution CLEAN–SC Beamforming," 7^{th} *Berlin Beamforming Conference, March 5 – 6 2018, Berlin, Germany*, GFaI, e.V., Berlin, 2018, BeBeC–2018–D07.

[67] G.R.A.S. Sound & Vibration – 42AA Pistonphone class 1, "https://www.gras.dk/products/calibration-equipment/reference-calibrator/product/255-42aa," Accessed in March 2017.

[68] VanDercreek, C. P., Avallone, F., Ragni, D., and Snellen, M., "Simulating the acoustic response of cavities to improve microphone array measurements in closed test section wind tunnels," *Journal of the Acoustical Society of America*, Vol. 151, No. 322, 2022, pp. 1–13.

[69] Visaton – Speaker K 50 SQ – 8 Ohm, "http://www.visaton.de/en/products/fullrange-systems/k-50-sq-8-ohm," Accessed in March 2017.

[70] Dougherty, R. P., "Cross Spectral Matrix Diagonal Optimization," 6^{th} *Berlin Beamforming Conference, February 29 – March 1, 2016, Berlin, Germany*, GFaI, e.V., Berlin, 2016, BeBeC–2016–S2.

[71] Brooks, T. F., Pope, D. S., and Marcolini, M. A., "Airfoil Self–Noise and Prediction," Tech. Rep. NASA Reference Publication 1218, NASA Reference Publication 1218, 1989.

[72] Lima Pereira, L. T., Merino-Martinez, R., Ragni, D., Gómez-Ariza, D., and Snellen, M., "Combining asynchronous microphone array measurements for enhanced acoustic imaging and volumetric source mapping," *Applied Acoustics*, Vol. 182, No. 108247, June 2021, pp. 1–24.